Available online at www.sciencedirect.com

ScienceDirect

journal homepage: www.elsevier.com/locate/he

An analysis of the imperfections and defects inside composite bipolar plates using X-Ray computer tomography and resistivity simulations

Michael Sietmann [a,b,*], *Holger Janßen* [a], *Martin Müller* [a], *Werner Lehnert* [a,b]

[a] *Forschungszentrum Jülich GmbH, Institute of Energy and Climate Research, Electrochemical Process Engineering (IEK-14), 52425, Jülich, Germany*

[b] *Modeling in Electrochemical Process Engineering, RWTH Aachen University, 52056, Aachen, Germany*

HIGHLIGHTS

- X-Ray computer tomography reveals the inner structure of composite bipolar plates.
- Cracks, air bubbles and agglomerations of foreign particles detected inside BPP.
- Imperfections inside BPP have minimal impact on the electric properties.
- The flow field has a major impact on the electrical resistance of composite BPP.

GRAPHICAL ABSTRACT

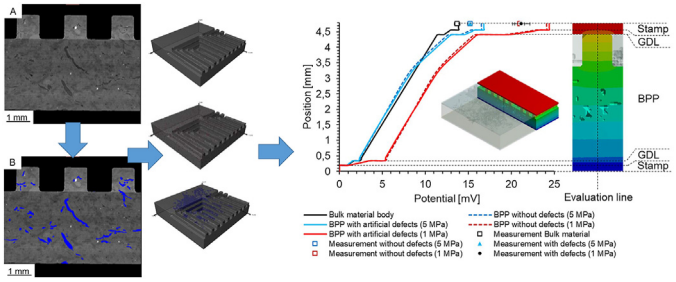

ARTICLE INFO

Article history:
Received 27 October 2020
Received in revised form
12 April 2021
Accepted 12 May 2021
Available online 5 June 2021

Keywords:
Bipolar plate
Imperfections
Defects
X-ray computer tomography
Resistivity simulation

ABSTRACT

With the increasing mass production, the quality control of bipolar plates (BPPs) becomes more important. A classification and understanding of imperfections and defects is necessary for the design of quality assurance measures within the manufacturing process. In this paper, a combined X-Ray computer tomography (CT) and resistivity simulation approach is used to investigate graphite composite BPPs. With this non-destructive approach, the morphology and composition of a detailed BPP section, as well as an entire flow field, can be analyzed for its characteristics and defects. The different detected imperfections occurring in injection-molded and compression-molded BPP samples include cracks, air bubbles and agglomerations of voids and foreign particles. The investigated flow field geometry has a major impact and increases the electrical resistance by about 19% compared to a bulk material body. The investigated imperfections inside the BPP material have a minimal impact on the electrical resistance of the BPP.

* *Corresponding author*. Forschungszentrum Jülich GmbH, Institute of Energy and Climate Research, Electrochemical Process Engineering (IEK-14), 52425, Jülich, Germany.
E-mail address: m.sietmann@fz-juelich.de (M. Sietmann).

https://doi.org/10.1016/j.ijhydene.2021.05.078

0360-3199/© 2021 The Author(s). Published by Elsevier Ltd on behalf of Hydrogen Energy Publications LLC. This is an open access article under the CC BY license (http://creativecommons.org/licenses/by/4.0/).

© 2021 The Author(s). Published by Elsevier Ltd on behalf of Hydrogen Energy Publications LLC. This is an open access article under the CC BY license (http://creativecommons.org/licenses/by/4.0/).

Introduction

In order to achieve broad commercialization, the production costs fuel cell systems must be reduced. In addition to the membrane electrode assembly (MEA), including the gas diffusion layer (GDL), the bipolar plate (BPP) is one of the fuel cell components with the highest cost reduction potential. Depending on the cost model and assumptions for produced numbers and stack size, the costs of bipolar plates are calculated as amounting to 45% [1], 29% [2] or 28% [3] of the overall fuel cell stack's costs. Despite the wide variation in cost assumptions, BPPs are responsible for a significant portion of fuel cell costs. Therefore, their cost-effective mass production is necessary [4]. The main properties of a BPP are a high gas impermeability, high electrical conductivity, high thermal conductivity, good mechanical and chemical stability and low production costs [5]. Target properties for BPPs in automotive applications have been set out by the U.S. Department of Energy (DOE) [6]. To meet all of the listed criteria for BPPs, composite BPPs of high quality must be produced. Possible materials for these in the purview of companies and researchers are metals and carbon composite materials. Metallic bipolar plates have superior electrical and thermal properties but are prone to corrosion and therefore require a protective coating [7]. More suitable for stationary applications with long lifetime requirements are carbon composite materials, but achieving high electrical conductivity values is an issue for those for BPPs [8]. In carbon composite materials, electrons are conducted through a percolating network of conductive filler materials, which Kreuz [9], for example, has clearly demonstrated. Dawson et al. [10] assume that the electrical resistance in composites with carbon black is dominated by the charge transfer across the insulating gaps between adjacent carbon black particles for low filler contents but that in highly loaded materials, the intra-particle processes becomes more dominant. Conductive filler materials that have been investigated for BPPs include natural and synthetic graphite, expanded graphite, carbon fibers, carbon black, carbon nanotubes and graphene [5,11–13]. In general, the electrical resistance decreases with the increase in conductive filler content. To meet the conductivity requirements, BPPs are highly loaded composites. Antunes et al. [14] list the results of different research groups that met the target property for the electrical conductivity of 100 S/cm in the in-plane direction, but not in the through-plane direction, whereas virtually only the in-plane conductivity was reported. Increasing graphite filler contents decrease the flowability of bulk-molding compounds and, for easy manufacturing, a specific amount of resin material is needed, as stated by Hsiao et al. [15]. Heo et al. [16] observed non-conducting regions made of resin material in their composites to block the connection of electrical conductive paths, increasing the overall resistance of the material. Antunes et al. [14] concluded that the percolation network can be reduced through the agglomeration of particles due to poor dispersion, leading to lower bulk conductivity of the BPP. Other possible non-conducting regions inside BPPs are voids, cracks and other foreign non-conductive particles. A better understanding of the influence of the defects and imperfections that can occur during the production process will help control and maintain the production of BPPs at a high level of quality. Anett et al. [17] used SEM on cryogen fracture surfaces of injection-molded and compression-molded BPP materials with different material compositions. They described core and skin regions in injection-molded samples in which width depends on the matrix material used and flow velocities. By removing the insulating skin region, the electrical conductivity could be increased. The effect of the production method on the internal BPP structure has also been reported in the literature [18,19]. Simaafrookhteh et al. [20] report on different defects that can occur during the compression molding of composite BPPs and how to mitigate these during the molding process. The investigated defects contain porosities inside the resin caused by volatiles and gases generated during the curing process, such as the bonding of materials due to poor material choices, delamination and crack formation and also the formation of patterns due to pre-curing. The influence of those defects on the electrical properties has not been reported in the literature. Using a special measurement cell, Baumann et al. [21] investigated different defect sites on the surface of a graphitic compound BPP between BPPs and GDLs, respectively, by evaluating the current distribution and transverse conductivity of the bulk materials. By increasing the defect area, the current below the defect decreases linearly. Müller et al. [22] used metal plates to detect cross-conductivities inside bipolar plates and used these as an indicator of defects in the MEA or other malfunctions in the fuel cell but did not link the transverse conductivities to defects inside the BPP.

This paper investigates the occurrence, dimensions and distribution of defects and imperfections inside composite BPPs by means of an X-Ray computer tomography (CT) approach and simulates the effect on electrical conductivity using a finite element method (FEM) simulation model. FEM simulation models have been used to predict the contact resistance between BPPs and GDLs under homogeneous and inhomogeneous contact pressure distributions [23–25] and to simulate the optimal flow field rib width and rib shapes, but the potential losses throughout the entire BPP and GDL were not investigated. Qiu, Peng [26] considered the material properties and used an analytical model to show the influence of BPP surface morphology and GDL compression on the contact resistance. Nevertheless, the internal structure of the BPP was not in the focus of their study. X-Ray CT is a non-destructive measuring method to investigate the inner

structure of materials and components [27,28]. Compared to scanning electron microscopy (SEM), X-Ray CT has the advantage that the sample requires no special preparation before measuring. In addition, 3D tomograms with higher information contents can be generated instead of 2D images [29]. Features like delamination, voids or matrix cracks can be visualized in 3D, avoiding possible misinterpretation from 2D characterization methods [30]. The X-Ray CT is widely used to detect defects and failure modes in polymers with carbon fibers, as they have a wide range of applications. Furthermore, the numerical reconstruction of the X-Ray CT data of fiber-reinforced polymer composites finds broad application in different simulation models [30–32]. To our knowledge, there has been little use of X-Ray CT in the investigation of composite materials for bipolar plates presented in the literature, especially including the numerical reconstruction of the data. Pilinski et al. [33] employed X-Ray tomography to show the surface changes of a BPP under fuel cell conditions. However, the inside of it was not investigated.

This paper first describes the X-ray computer tomography setup and segmentation methods undertaken, followed by the setups for the electrical resistivity measurements and resistivity simulations. The electrical resistivity measurements are used to obtain input data for the resistivity simulation. To measure the specific through plane resistivity of a graphite BPP, Kakati, Sathiyamoorthy [34] applied the four-probe technique commonly used for in-plane measurements to a through-plane measurement. With their setup, Kakati, Sathiyamoorthy [34] showed the increasing conductivity with increasing filler content. They were also able to identify an optimum amount for a second filler. Dhakate, Sharma [35] used a sandwich setup of GDL and BPP under mechanical force to measure and compare the through-plane resistances of BPP with different filler content. To obtain the specific through-plane resistivity of the BPP, BPP samples with different thickness have to be measured and compared as shown by Cunningham, Lefèvre [36] and Sadeghifar [37]. Imperfections detectable with the X-Ray CT approach are presented and analyzed. BPP with artificial imperfections are then investigated with a simulation model generated from X-Ray CT data to reveal the change in the potential distribution within the BPP due to imperfections. The simulation results show the influence of BPP geometry and imperfections inside the BPP on overall electrical resistivity.

Experiments and simulation setup

X-ray computer tomography

For our investigations, we use a high-resolution CT Xradia 410 Versa from Carl Zeiss AG. This CT uses a two-stage magnification architecture with geometric and optical magnification. The geometric magnification is achieved via adjustable distances between the source, sample and detector. For the optical magnification, lenses between a 0.4x and 40x zoom are available. With this CT we have, on the one hand, the opportunity to investigate the entire flow field of an example BPP with a dimension of 42 mm × 42 mm and a resolution of 30 μm–40 μm per pixel. At lower magnification, the entire active area can be scanned for larger defects. On the other hand, at higher magnification it is possible to obtain a resolution at the nanometer scale, making the morphology of the BPP visible. Using the high magnification, a region of only a few millimeters can be investigated. The CT software generates a grey level tomogram of the sample, depending on the transmission of the X-Rays. The evaluation software used for the grey scale tomograms was DragonFly by ORS. In the evaluation software, strongly absorbing materials are shown in brighter grey levels and less absorbing materials in darker grey ones. The X-Ray absorption of materials can be expressed with the absorption coefficient μ, which depends on the elements of the material, expressed by the atomic number Z, the density of the material ρ, the energy of the photons produced by the X-Ray source E and a constant K [30]:

$$\mu = K \cdot \rho \cdot \frac{Z^4}{E^3} \tag{1}$$

Material assignment with X-Ray computer tomography

The absorption coefficient for X-Rays is proportional to the atomic number to the power of four and to the density of the material (Eq. (1)). This can be used to differentiate materials inside the BPP. Graphite is composed of carbon atoms and the polymer binder, used in BPP, also consists mainly of carbon atoms, making it challenging to differentiate between the two materials based on the absorption coefficient. The investigated BPP material samples use different polymer binders, i.e., polypropylene (PP), polyvinylidene fluoride (PVDF) or polyphenylene sulfide (PPS). The difference in the density of PPS binder materials and graphite is sufficient to see a slight difference in the greyscale image of a tomogram. Fig. 1 shows a higher magnification resolution for the greyscale image of a sample with a known material composition, as listed in Table 1. For the better calibration of the material segmentation, a total of 10% magnesium oxide is added to the BPP material sample. Based on greyscale threshold values, the sample is segmented into areas assigned to the materials: graphite particles, polymer binder material, foreign particles and voids. The threshold values are set by comparing the intensity values of different particles at different locations in the tomogram. The intensity values range from a minimum of 1563 to a maximum of 65,314. The voids or air bubbles inside the sample absorb the X-Rays the least, and therefore an intensity range from the minimum of 1563 to a value of 4500 is assigned to them. The polymer material (marked in green) slightly absorbs less X-Rays than the graphite particles (red), and so this material is represented by the intensity values of 4501–8000 and 8001 to 11,000, respectively. The foreign particles absorb the X-Rays the best, leading to their assignment to the intensity values from 11,001 to the maximum of 65,314 (blue).

Table 1 lists the greyscale ranges and shows the comparison between the volume shares of original material composition and the material composition based on greyscale interpretation. Due to the slightly inaccurate setting of

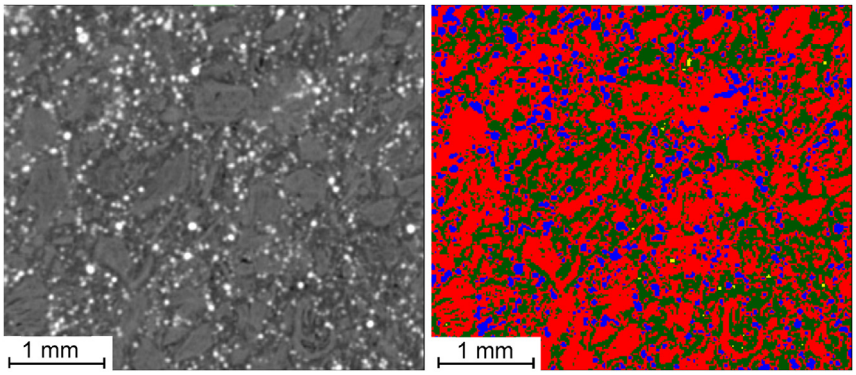

Fig. 1 – Material assignment of graphite particles (red), polymer binders (green), foreign particles (blue) and voids (yellow) based on their intensity values. (For interpretation of the references to color in this figure legend, the reader is referred to the Web version of this article.)

Table 1 – Composition of example BPP material with added MgO particles.

Segment	Intensity value	Volume share (CT) in %	Volume share (manufacturer information) in %
Graphite	8001–11,000	57.7	60
Polymer binder	4501–8000	32.7	30
Particles (MgO)	11,000–65,314 (max)	9.5	10
Air bubbles	1563 (min) - 4500	0.1	0

thresholds and only investigating details of the produced sample, the shares of the CT-based interpretation vary somewhat from the original material composition. This evaluation method for composite BPP material shows only trends; nevertheless it can be applied to BPP to locally determine the shares of graphite particles and polymer binder material.

Electrical resistivity simulation

To simulate the influence of the defects on the electrical resistance, a 2 cm × 2 cm section from a larger composite BPP was investigated. The BPP samples have a thickness of 4 mm and the flow field consists of 1 mm-wide and 1 mm-deep channels, as well as 1 mm-wide ribs. An accurate CAD model of the section was developed using the 3D X-ray tomography data. With the software Dragonfly by ORS, surface meshes of the characteristics of the inner structure of the graphite composite bipolar plate could be generated. All voxels belonging to the BPP bulk material were marked and the imperfections spared out. Then, a surface mesh of the outline of the marked voxels was automatically generated by the software. The graphite particles could not be separated from their surroundings with the resolution used for the X-ray investigation of a 4 cm^2 area. For the simulations, the bulk material was assumed to be homogeneous. The imperfections were simulated as non-conductive particles.

For the electrical resistivity simulation carried out for this study, an ANSYS Mechanical solver was used. The DragonFly surface mesh could not be used directly for the simulation, because of the additional bodies for the current contact body and the GDL that were added on top of and below the investigated BPP according to the experimental investigation and validation for the simulation. Therefore, the software SpaceClaim was used to transform the mesh into a solid body again and revise its geometry. The edited geometry was meshed with the ANSYS meshing tool. A hexagonal mesh was used for the GDL and the gold stamps, which represent the current contact bodies, and a tetrahedral mesh was used for the BPP. In total, the computational mesh consists of about 500,000 elements.

For the calculation of the electrical potential distribution, an equation for the steady-state conduction was used with the potential V and electrical conductivity matrix $[\sigma]$:

$$-\nabla \cdot ([\sigma]\nabla V) = 0 \tag{2}$$

The electrical conductivity matrix $[\sigma]$ consists of two in-plane resistances and the through-plane resistance. The potential drop ΔV at an electric contact surface is calculated with the electric contact conductivity *ecc* and the current density J:

$$\Delta V = \frac{J}{ecc} \tag{3}$$

Contact models for the contact areas of the GDL are substituted by an empirical value *ecc* depending on the contact pressure in the system.

The simulation results of the electric potential simulation are evaluated along a line through the model. For ANSYS, to calculate the local electric potentials along a line through the model, surfaces for the evaluation have to be defined. Therefore, small cuboids are implemented into the simulation model. Fig. 2 is showing a section of the simulation model with the cuboids in it. In each regime the cuboids have the same properties as the GDL, the BPP and the stamp without contact resistances to their neighboring bodies within their regimes. As boundary conditions a current density of 1 A/cm^2 was applied to the top surface of the current contact bodies, while a potential of 0 V was applied to the bottom surface of the other current contact bodies. The golden stamps were simulated as 200 μm-thick bulk bodies and the GDL as 150 μm thick bulk bodies in this model. The specific electrical

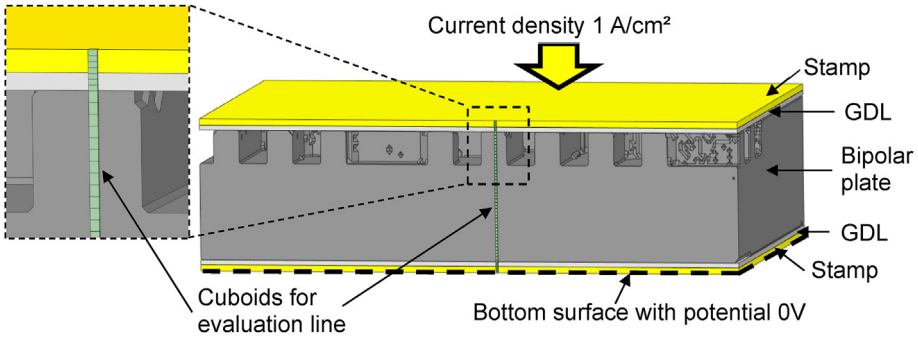

Fig. 2 – Section through simulation model with representation of the additional cuboids for evaluation.

Table 2 – Through-plane resistivities, in-plane resistivities and contact conductivities.

Material \ Compression Pressure	Through-plane resistivity		In-plane resistivity
	1 MPa	5 MPa	
BPP	22.84 mΩcm	22.17 mΩcm	8.90 mΩcm
GDL	186.6 mΩcm	57.27 mΩcm	9.57 mΩcm
	Contact conductivity		
Contact GDL-Stamp	9.32 S/mm²	11.43 S/mm²	
Contact BPP-GDL	5.79 S/mm²	14.65 S/mm²	

resistances of the golden stamps were set to 0,017 mΩcm. The specific through-plane resistivity, in-plane resistivity and the contact resistances of the materials for the BPP and GDL were determined experimentally and their values are listed in Table 2 in the result section. The contact type between GDL and golden stamp and between BPP and GDL were set to 'bonded' with a manually given value for the electric conductivity as listed in Table 2.

Four different simulations were carried out:

- Simulation of a bulk material body without a flow-field
- Simulation of an ideal BPP sample with a flow-field, serving as the reference model
- Simulation of a BPP sample where only separated and randomly placed foreign particles with a diameter of a few μm and a volume share of 0.04% were considered as imperfections
- Simulation where only intentionally-placed wooden particles inside the BPP with dimensions of up to several hundred μm and a volume share of 1.6% were taken into account as imperfections.

For the three simulations of the BPP, the same X-Ray tomogram was considered, therefore the outer shape is equal for those simulations. The voxels representing the imperfections in the X-Ray tomogram accounted for the bulk of the material for the reference model and the simulation of the BPP with imperfections, where they were treated as non-conductive particles.

Resistivity experiments

The in-plane and through-plane resistivity of the bulk BPP material are needed for the electric simulation to determine changes in ohmic losses due to imperfections and defects in the BPP.

For the in-plane resistivity measurement, a four-point probe technique is used. The BPP material samples are connected with a copper plate on each side along the entire length. A current is then applied to the BPP via copper contacts. The potential is measured at different distances on a straight line that was placed vertical to the copper plates. The specific in-plane resistivity ρ_{ip}can be calculated with Eq. (4), where U is the measured potential, I the current,A the surface connected to the current source and $L$the distance between the needles that measure the potential difference. The specific through-plane resistivity ρ_{tp} is calculated with the thickness d of the sample (Eq. (5)):

$$\rho_{ip} = \frac{U}{I} \cdot \frac{A}{L} \tag{4}$$

$$\rho_{tp} = \frac{U}{I} \cdot \frac{A}{d} \tag{5}$$

Fig. 3 shows a schematic representation of the experimental setup for the in-plane measurements and the experimental setups for the through-plane measurements. The current for the in-plane and through-plane experiments was applied through a Gossen Konstanter and measured with a Fluke 45 dual display multimeter. The potential was also measured in all experiments with a Fluke 45 dual display multimeter. For the through-plane resistivity and contact resistance measurements, BPP material samples with dimensions of 2 cm × 2 cm were cut out of a larger BPP. A PWV 2 EH-Servo hydraulic press was used to apply the compression force and different experimental setups were investigated.

To determine the bulk resistivity and contact resistances of the GDL, the experimental method proposed by Sow et al. [38] is adapted. A copper foil is placed between two 100 μm-thick insulating foils and two BPP samples. This composition is placed on a GDL and then connected with golden stamps from both sides (see Fig. 3). The voltage difference between the

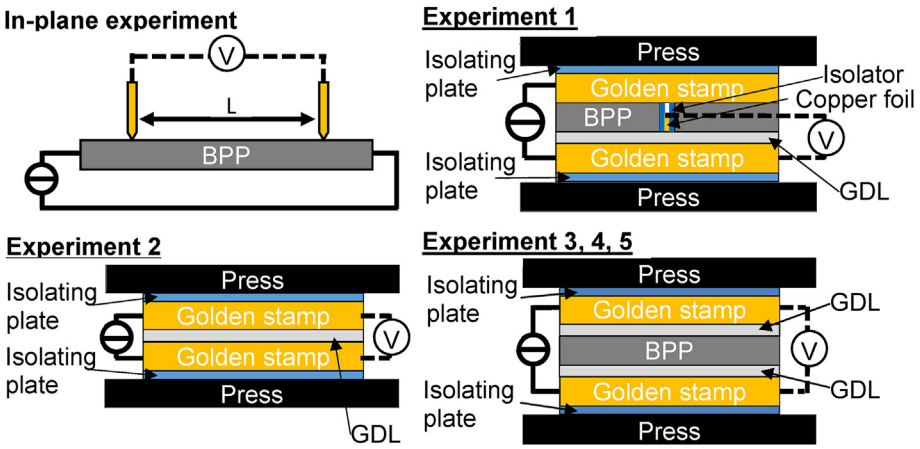

Fig. 3 – In-plane measurement setup (top left) and through-plane measurement setups: experiment 1 with one GDL and contact through copper foil (top-right); experiment 2 with one GDL (bottom-left); experiments 3–5 for BPPs with different thicknesses (bottom-right).

copper foil and the bottom golden stamp is measured, which yields a potential drop consisting of the contact resistance between the golden stamp and GDL plus the bulk resistance of the GDL. As Sow et al. [38] note, the measured voltage drop will not be accurate due to the bending of equal potential lines along the corners of the connecting BPPs. In a second experimental setup, the GDL is placed between golden stamps and the potential drop caused by two times the contact resistance of the golden stamp and GDL, with the bulk resistance of the GDL also being measured (see Fig. 3). The experimental setup to evaluate the bulk resistivity of the BPP material is shown in Fig. 3 at the bottom-right and consists of two golden stamps, two GDLs and a BPP sample milled to a thickness of 2 mm and one to a thickness of 3 mm, respectively. Finally, the original BPP material with a thickness of 4 mm is placed with a GDL on each side between the golden stamps to measure the total resistance of the reference BPP, because slightly different surfaces compared to the original BPP are observed on the down-milled material samples. This was performed to compare the overall potential of a bulk material cutout with cutouts of the BPP flow-field of the same material. The experiments were repeated several times to determine an average value for each of them. The different experimental setups led to a linear system of equations in which the bulk

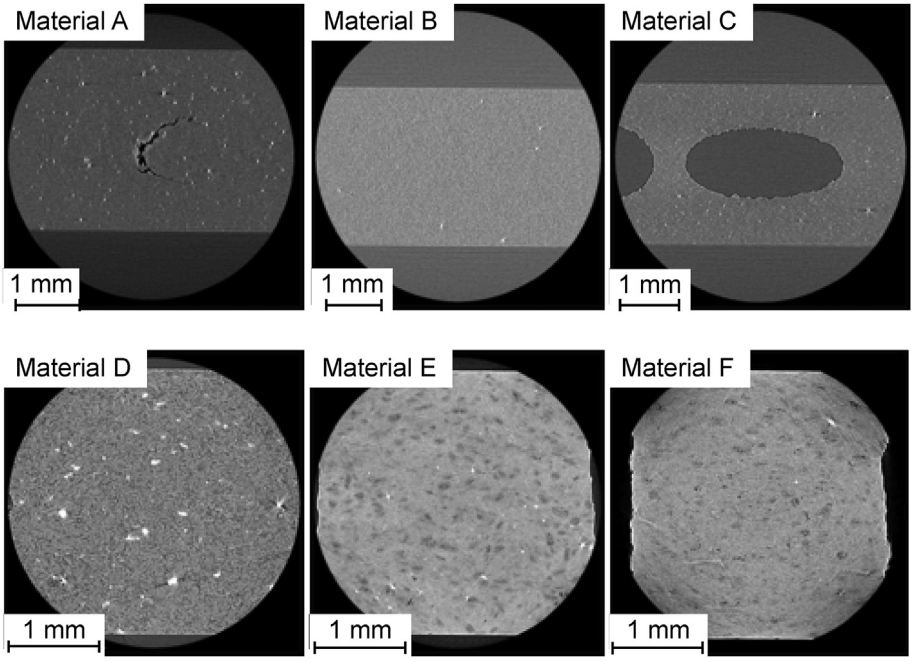

Fig. 4 – X-Ray CT cross-section of six material samples. Material A: injection-molded BPP material with a large crack; Material B: injection-molded BPP with almost no imperfections; Material C: injection-molded BPP with large air bubbles; Material D: compression-molded BPP with large graphite particles and foreign particles; materials E and F: compression-molded BPP with agglomerations of polymer binder or voids.

resistivity of the BPP material, the GDL material and contact resistances of the gold stamp-GDL and BPP-GDL, respectively, could be calculated. The equations, with their measured overall potential differences, are listed below:

$$\text{Exp.1:} U_1 = 1\cdot U_{GDL} + 1\cdot U_{Contact\ GDL,Stamp} + 0\cdot U_{Contact\ GDL,BPP} + 0\cdot U_{BPP} \quad (6)$$

$$\text{Exp.2:}\ U_2 = 1\cdot U_{GDL} + 2\cdot U_{Contact\ GDL,Stamp} + 0\cdot U_{Contact\ GDL,BPP} + 0\cdot U_{BPP} \quad (7)$$

$$\text{Exp.3:}\ U_3 = 2\cdot U_{GDL} + 2\cdot U_{Contact\ GDL,Stamp} + 2\cdot U_{Contact\ GDL,BPP} + 1\cdot U_{BPP,2mm} \quad (8)$$

$$\text{Exp.4:}\ U_4 = 2\cdot U_{GDL} + 2\cdot U_{Contact\ GDL,Stamp} + 2\cdot U_{Contact\ GDL,BPP} + 1\cdot U_{BPP,3mm} \quad (9)$$

$$\text{Exp.5:}\ U_5 = 2\cdot U_{GDL} + 2\cdot U_{Contact\ GDL,Stamp} + 2\cdot U_{Contact\ GDL,BPP} + 1\cdot U_{BPP,4mm} \quad (10)$$

The specific through-plane bulk resistances (compare Eq. (5)) of the BPP and the GDL as well as the contact conductivities for the simulation model (compare Eq. (3)) can be calculated using Eqs. (6)–(10). The mean values of at least ten measurements are used for calculating the simulation parameters:

$$ecc_{GDL,Stamp} = J\cdot\frac{1}{U_2 - U_1} \quad (11)$$

$$\rho_{tp,BPP} = \frac{U_4 - U_3}{d_{BPP,3mm} - d_{BPP,2mm}}\cdot\frac{1}{J} \quad (12)$$

$$\rho_{tp,GDL} = \frac{1}{J\cdot d_{GDL}}\cdot\left(U_1 - J\cdot\frac{1}{ecc_{GDL,Stamp}}\right) \quad (13)$$

$$ecc_{GDL,BPP} = J\cdot\frac{2}{U_5 - J\cdot\left(2\cdot\rho_{tp,GDL}\cdot d_{GDL} + \frac{2}{ecc_{GDL,Stamp}} + \rho_{tp,BPP}\cdot d_{BPP,4mm}\right)} \quad (14)$$

Results and discussion

Detectable imperfections

As described by Simaafrookhteh et al. [20], during the production of composite materials for BPPs, different problems can occur, such as delamination or trapped gases. To enhance the detectability of those defects with the X-Ray tomography approach, six different material samples made of different polymer binder and graphite filler combinations were investigated. The material samples were provided by two different suppliers; their exact material composition will not be stated in this paper. 2D sections from X-Ray tomograms belonging to the six different samples are shown in Fig. 4. Samples A-C were produced by an injection molding process while samples D-F were produced by a compression molding process. In the grey level tomogram, the BPP materials clearly differ from the surrounding air because their carbon content absorbs more of the X-Ray radiation. The six 2D sections show different failure modes that can occur inside a graphite composite BPP. A direct comparison of the samples is difficult because of the different grey level changes due to different sample sizes, X-Ray CT settings and post processing with the evaluation software. Sample A shows a large crack in the middle of the object. This crack absorbs fewer X-Rays and therefore it is shown in darker colors than the surrounding carbon and binder materials. Foreign particles that do not belong to the graphite composite are shown as white particles and can be seen in almost every investigated sample. These particles consist of elements that absorb the X-Rays even better than the graphite or polymer binder material. Sample B has no larger defects visible in the presented section. The material seems to be fairly homogeneous and only has a few foreign particles. Large air bubbles can also occur during the injection molding process, as detected in sample C. The air bubble has a diameter larger than 1 mm, which is more than one third the thickness of the material sample. Sample D is made of larger graphite particles, and so the entire inner structure with the composition of the particles can be made visible at lower magnification. Larger foreign particles can interrupt the connection between two or more adjacent graphite particles. This will reduce the number of conductivity pathways if the foreign particles are non-conductive. Therefore, foreign particles can lead to an increase in the electric resistivity. Samples E and F show agglomerations of voids and small air bubbles inside the BPP materials and a small number of foreign particles. The agglomerations of voids are distributed randomly across the entire sample.

EDX analysis of the different samples indicated that the foreign particles were primarily aluminum silicates and calcium silicates, prompting the assumption that the particles enter the manufacturing process with the raw materials. In some material samples, foreign particles with a high iron content could also be observed.

Distribution of imperfections

The material assignment is applied to the six material samples shown in the previous section. With this approach, a statistical evaluation of the size and number of imperfections can be generated. The distribution of the imperfection sizes in the six investigated material samples is shown in Fig. 5. The results show that in those samples there are many small foreign particles and a few larger imperfections. For a better comparison and visualization, the imperfections are treated as spherical volumes and the equivalent diameter based on the shape of a sphere is calculated. The only defects or imperfections considered are those that have an equivalent diameter larger than 10 μm and which can be clearly differentiated from the surrounding matrix by the evaluation software. In a sample volume of 13.6 mm^3, there can be up to 10,000 micro-sized imperfections such as foreign particles, voids or air bubbles with an equivalent diameter of less than

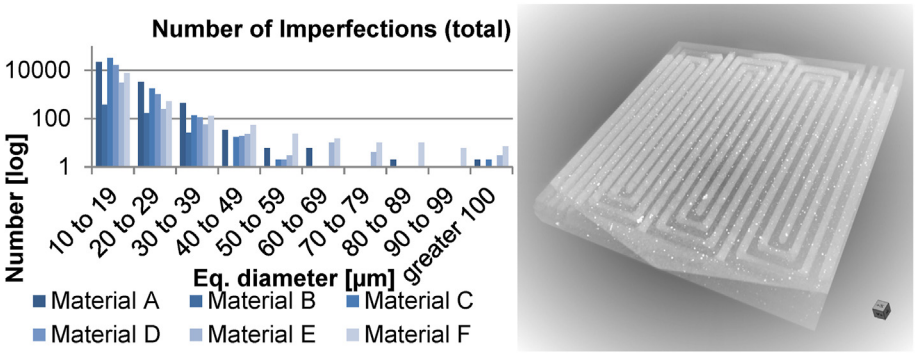

Fig. 5 – Particle size distribution of material samples (left); spatial distribution of foreign particles in a sample BPP (right).

20 µm. Larger imperfections like cracks or large air bubbles only occur in small numbers and can only be seen in some of the investigated material samples.

For the spatial distribution inside a BPP, an entire flow-field with the dimensions of 42 × 42 mm^2 was investigated. The BPP is a compression-molded sample with a thickness of 4 mm while the channels of the flow-field have a width and depth of 1 mm. The resolution of the CT scan is about 35 µm per voxel. To show the inner properties of the right-hand picture in Fig. 5, the transparency of the greyscale image was increased. The foreign particles inside the BPP material become visible in large numbers in the transparent BPP image. They are randomly distributed across the entire BPP. This leads to the assumption that they are added to the BPP material with the raw material or at the mixing stage of the polymer binder with the graphite particles.

Resistivity measurements

The measurement results for the area-specific in-plane and through-plane resistances of the BPP material and of the GDL used are shown in Fig. 6. The potential differences increase linearly with the increasing distance between the measurement points, and therefore the specific in-plane resistivity as shown in Eq. (4) can be directly calculated from the slope of the graphs. The through-plane resistivities and contact conductivities can be calculated according Eq. (11)–(14). The results for the specific resistances used in the simulations are listed in Table 2. Fig. 6 also shows the measurement results of BPP with and without defects for comparison with the simulation results, presented in section Simulation results.

In accordance with Qiu et al. [39], the through-plane resistivity experiments show that the change in the total resistance of the GDL and BPP with increasing pressure is becoming minimal, reducing the deviation in the simulation parameters for higher compression pressures.

The measured resistance for experiment 1 is only an approximation for the GDL bulk resistance and the contact resistance due to the gap between the current-conducting BPP and measurement foil. A detailed explanation of this inaccuracy is provided by Sow et al. [38], who used thinner measurement tips and insulating foils, leading to an inaccuracy of less than 11%. The specific resistances were calculated for a compression pressure of 1 MPa and 5 MPa from the measurement data and used as the simulation parameters. The inaccuracy of the measurement results for 1 MPa can play a role, as the simulation parameter can change rapidly with deviations in the measurement results. For the calculation of the GDL bulk resistance, a thickness of 150 µm is assumed for all compression pressures. The simulation input parameter for the electrical through-plane resistances of the GDL decreases with increasing compression pressure. The through-plane resistances for the BPP only changed slightly due to measurement uncertainties, and therefore are assumed to be constant in the simulation for all compression pressures. The contact resistance between the golden stamps and GDL, as well as the contact resistance between the GDL and BPP, also decrease with increasing compression pressure.

X-Ray investigation of BPP with artificial imperfections

With a high resolution of the X-Ray CT, only a small section of a BPP can be investigated. A BPP with artificial imperfections at a known location can be produced by a supplier to reduce the X-Ray CT scanning time and the search time for defects. Intentionally implemented wood particles are used to simulate imperfections such as cracks or large foreign particles. The wood particles were added to the composite material before compression-molding at the mixing stage so that they could distribute in the material. The wood particles are only implemented on one side of the BPP, allowing a comparison with the imperfection-free symmetrical other half of the same BPP. In the X-Ray CT images, the implemented wood particles can be clearly seen and extracted by the methods described in the previous sections. The wood particles absorb fewer X-Rays than the graphite or polymer matrix present in the BPP material sample. The interpretation of the grey scale image and marking of the wood particles in blue is shown in Fig. 7A and B. The wood particles are distributed across the entire height of the sample, differ in size and orientation and the volume share of the BPP material in the investigated area is about 1.6%. The investigated area of the BPP was about 4 cm^2, allowing a resolution with the CT to detect all wood particles. Fig. 7C–E show the outlines of the reference model, the model with randomly-placed foreign particles and that with wood particles that are generated from the X-Ray data of a real BPP sample.

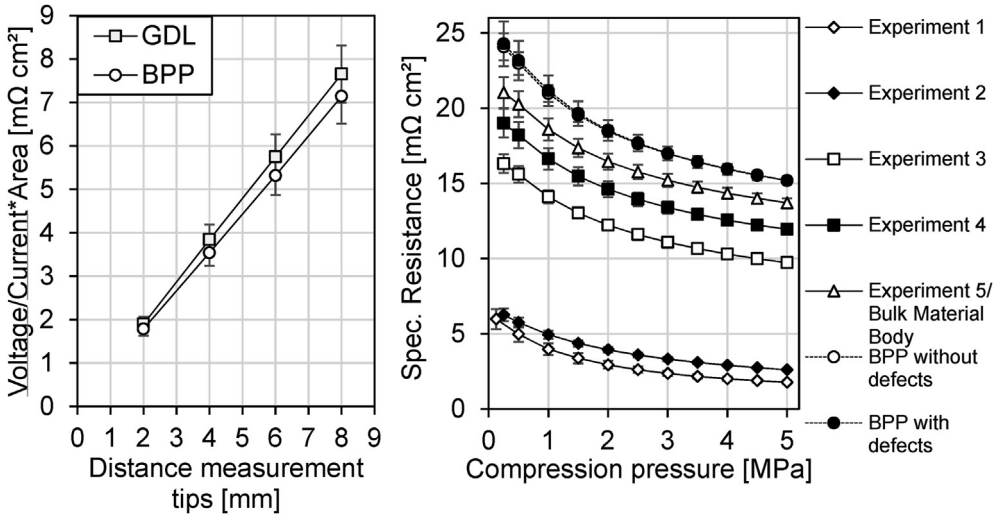

Fig. 6 – In-plane specific resistances for GDLs and BPPs measured with respect to the distance between measurement points (left) and through-plane-specific resistances measured for different experimental setups with respect to compression pressure (right).

Simulation results

Fig. 8 shows a section of the simulation results and the location of the evaluation line for the potential drop in the model on the right.

Fig. 8 shows the voltage losses through the simulation model of a BPP bulk material sample, an ideal BPP sample with a flow field and one with artificial imperfections for a compression pressure of 1 MPa and 5 MPa, respectively. The losses due to contact resistance are represented through horizontal lines in the potential curve. In the contact body there is no voltage loss due to the high electrical conductivity of the golden stamp. The upper GDL, which is in contact with the flow-field side of the BPP and the contact resistances on this side are responsible for a voltage loss of 3.73 mV, assuming a compression pressure of 5 MPa. This is equivalent to 22.6% of the total voltage loss in the simulation model for the ideal BPP. The contact loss between the upper GDL and BPP is overestimated in the simulation model with the flow-field because it only considers the smaller contact surface due to the flow field structure, but not the better conductivity inside the GDL and at the contact surface due to higher contact pressure on the flow-field ribs. The contact loss of the bottom GDL with the BPP is lower in the simulation model compared to the upper contact surface with respect to a larger contact area. At a compression pressure of 5 MPa, the main share of the voltage loss is due to the bulk losses inside the BPP, with a voltage drop of 10.5 mV, which means a loss of 63.6% of the total voltage loss. The bulk losses inside the BPP can be divided into three sections, two of which are linear, as well as a

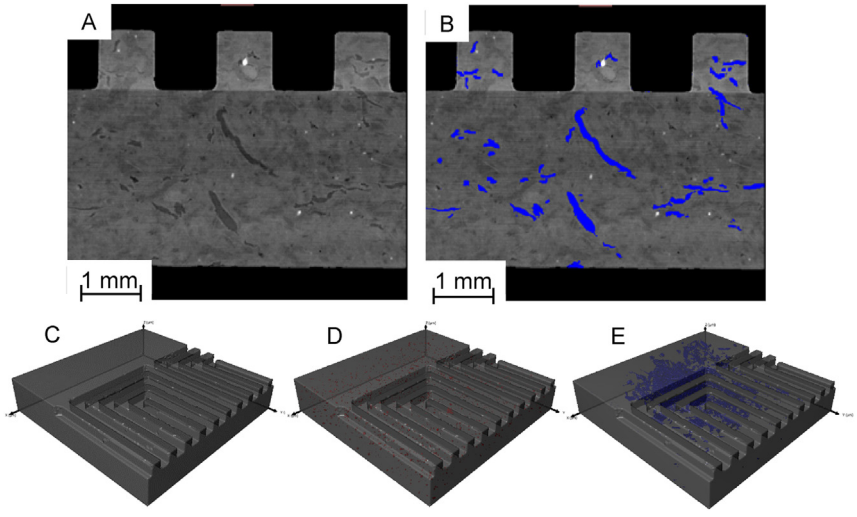

Fig. 7 – Interpretation of the grey scale image and marking of wood particles in blue (Images A and B). 3D models generated from X-Ray data: ideal sample without imperfections (Image C); sample with foreign particles marked in red (Image D); and sample with wood particles marked in blue (Image E). (For interpretation of the references to color in this figure legend, the reader is referred to the Web version of this article.)

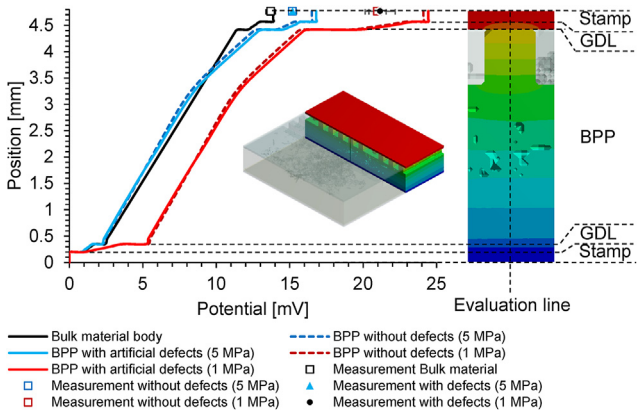

Fig. 8 – Potential distribution inside the simulation model along the evaluation line for ideal BPP samples and BPP samples with artificial wood particles at 1 MPa and 5 MPa compression pressures, respectively (left); and cross-section with evaluation line (right).

transition section. The first linear section with the larger slope starting around the position 0.35 mm represents the potential drop in the bulk body regime while the second linear section represents the potential drop in the flow field regime of the BPP. The bulk material sample is simulated as a homogeneous material and has the same slope all over the sample. The flow field also affects the potential drop at the contact surface to the GDL, the potential distribution and potential drop in the GDL itself. Related to a full bulk material sample, the BPP with the flow-field has a 19.0% higher potential drop at the same current density.

In the ideal sample, a voltage drop of 10.5 mV over the BPP and of 16.5 mV over the entire simulation model at a current density of 1 A/cm^2 was simulated. In the simulation model with wood particles, the voltage drop over the BPP increases to 10.91 mV and through the entire model to 16.81 mV. This is an increase of 0.41 mV (+3.9%) and 0.31 mV (+1.9%), respectively. The sample with small foreign particles shows nearly no increase in the simulated voltage drop over the BPP body model nor the entire model, increasing it by 0.02 mV (+0.2%) and 0.07 mV (+0.4%), respectively. For better clarity of the graphs, this sample is not shown in Fig. 8.

Considering the measurement uncertainties presented in Fig. 6 and the rapid decrease in contact resistances with increasing compression pressure, the effect of the artificial imperfections plays an even more subordinate role. A simulation of 1 MPa compression pressure, a more common pressure in the context of PEM Fuel cells, shows the declining effect. At a pressure of 1 MPa, the potential losses due to contact resistances and the bulk resistance of GDL on the flowfield side of the BPP are responsible for 8.29 mV (34.4%). The share of the BPP at the total potential losses decreases to 43.5% and the potential increase due to the artificial imperfection decreases to 1.4%.

In addition to the simulation results, Fig. 8 also shows the measurement results of the simulated setup for compression pressures of 1 MPa and 5 MPa. With the measurement setups, only the total potential loss can be measured. The measurement results are in good agreement with the simulation results for the BPP bulk body. At a current density of 1 A/cm^2 and a compression pressure of 5 MPa, implemented with the hydraulic press, the measured potential drop for the through-plane measurement setup on a bulk material sample is 13.72 mV. The deviation between the measurement and simulation result is 0.6%. For the BPP with a flow field and without defects, a potential drop of 15.18 mV is measured while for the BPP sample with implemented wood particles, a potential drop of 15.19 mV is measured. The deviation between simulation and measurement is larger for a BPP with flow field than for a bulk body due to the above mentioned overestimation of the contact resistance. Nevertheless, the results show the small influence of imperfections in the BPP. The measurement results in Fig. 6 also show that the influence of the separate investigated imperfections is negligible and cannot be accurately measured.

Conclusion

With the X-Ray computer tomography approach, the morphology of the graphite composite bipolar plates can be made visible and imperfections smaller than a few micrometers can be detected without destroying the sample. As the CT scan takes several hours to complete, this device can only be used for quality control in random samples. The development of a CAD model from the CT data with subsequent electrical resistivity simulation determines the component properties. This approach can be a useful tool in the development of future quality measurement instruments, or of composite BPPs, by showing the influence of imperfections on the material. Single and distributed foreign non-conductive particles a few micrometers in size and volume shares of around 0.04 vol.-% of the BPP volume do not affect the electrical resistivity of the BPP material. The in-plane resistivity of the BPP compensates possible blocked through-plane resistivity pathways. Larger amounts of imperfections of around 1.6 vol.-% with imperfections of several hundred micrometers in size can have a negative impact on the electrical resistivity of the carbon composite BPP. As simulated, they can increase the electrical resistance by almost 4%, for a compression pressure of 5 MPa, whereas in validation experiments they show no influence. Furthermore, the influence of defects in BPP decreases for lower compression pressures, as the contact resistances of the GDL and BPP increase. The flow field structure itself plays an overriding role compared to the influence of imperfections in the BPP, as the flow field increases the electrical resistance by almost 20% for the graphite composite BPP geometry investigated.

Declaration of competing interest

The authors declare that they have no known competing financial interests or personal relationships that could have appeared to influence the work reported in this paper.

Acknowledgements

This work was supported by the German Federal Ministry of Transport and Digital Infrastructure within the BePPel Project (Grant No. 03B11002D/03B11002D2).

REFERENCES

[1] Tsuchiya H, Kobayashi O. Mass production cost of PEM fuel cell by learning curve. Int J Hydrogen Energy 2004;29:985–90.
[2] Bar-On I, Kirchain R, Roth R. Technical cost analysis for PEM fuel cells. J Power Sources 2002;109:71–5.
[3] Wilson Ak G, Papageorgopoulos D. Fuel cell system cost. Department of Energy; 2017.
[4] Hermann A, Chaudhuri T, Spagnol P. Bipolar plates for PEM fuel cells: a review. Int J Hydrogen Energy 2005;30:1297–302.
[5] Taherian R. A review of composite and metallic bipolar plates in proton exchange membrane fuel cell: materials, fabrication, and material selection. J Power Sources 2014;265:370–90.
[6] Kopasz JPB, Thomas G. 2017 bipolar plate workshop summary report. Fuel Cell Technologies Office, U.S. Department of Energy; 2017.
[7] Tawfik H, Hung Y, Mahajan D. Metal bipolar plates for PEM fuel cell—a review. J Power Sources 2007;163:755–67.
[8] Alo OA, Otunniyi IO, Pienaar H, Iyuke SE. Materials for bipolar plates in polymer electrolyte membrane fuel cell: performance criteria and current benchmarks. Procedia Manufacturing 2017;7:395–401.
[9] Kreuz C. PEM-Brennstoffzellen mit spritzgegossenen Bipolarplatten aus hochgefülltem Graphit-Compound [Dissertation]. Universität Duisburg-Essen; 2008.
[10] Dawson JC, Adkins CJ. Conduction mechanisms in carbon-loaded composites. J Phys Condens Matter 1996;8:8321–38.
[11] Planes E, Flandin L, Alberola N. Polymer composites bipolar plates for PEMFCs. Energy Procedia 2012;20:311–23.
[12] Greenwood P, Thring RH, Chen R. Conductive materials for polymeric bipolar plates: electrical, thermal and mechanical properties of polyethylene-carbon black/graphite/magnetite blends. Proc IME J Mater Des Appl 2013;227:226–42.
[13] Lee JH, Jang YK, Hong CE, Kim NH, Li P, Lee HK. Effect of carbon fillers on properties of polymer composite bipolar plates of fuel cells. J Power Sources 2009;193:523–9.
[14] Antunes RA, de Oliveira MCL, Ett G, Ett V. Carbon materials in composite bipolar plates for polymer electrolyte membrane fuel cells: a review of the main challenges to improve electrical performance. J Power Sources 2011;196:2945–61.
[15] Hsiao M-C, Liao S-H, Yen M-Y, Su A, Wu IT, Hsiao M-H, et al. Effect of graphite sizes and carbon nanotubes content on flowability of bulk-molding compound and formability of the composite bipolar plate for fuel cell. J Power Sources 2010;195:5645–50.
[16] Heo SI, Yun JC, Oh KS, Han KS. Influence of particle size and shape on electrical and mechanical properties of graphite reinforced conductive polymer composites for the bipolar plate of PEM fuel cells. Adv Compos Mater 2006;15:115–26.
[17] Anett K, Ferenc R. Effect of processing technology on the morphological, mechanical and electrical properties of conductive polymer composites. J Polym Eng 2013;33:691–9.
[18] Derieth T, Bandlamudi G, Beckhaus P, Kreuz C, Mahlendorf F, Heinzel A. Development of highly filled graphite compounds as bipolar plate materials for low and high temperature PEM fuel cells. J N Mater Electrochem Syst 2008;11:21–9.
[19] Mighri F, Huneault MA, Champagne MF. Electrically conductive thermoplastic blends for injection and compression molding of bipolar plates in the fuel cell application. Polym Eng Sci 2004;44:1755–65.
[20] Simaafrookhteh S, Khorshidian M, Momenifar M. Fabrication of multi-filler thermoset-based composite bipolar plates for PEMFCs applications: molding defects and properties characterizations. Int J Hydrogen Energy 2020;45(27):14119–32.
[21] Baumann N, Blankenship A, Dorn M, Cremers C. Evaluating current distribution and influence of defect sites for graphitic compound bipolar plate materials. Fuel Cell 2020;20:40–7.
[22] Müller M, Hirschfeld J, Lambertz R, Schulze Lohoff A, Lustfeld H, Pfeifer H, et al. Validation of a novel method for detecting and stabilizing malfunctioning areas in fuel cell stacks. J Power Sources 2014;272:225–32.
[23] Lai X, Liu Da, Peng L, Ni J. A mechanical–electrical finite element method model for predicting contact resistance between bipolar plate and gas diffusion layer in PEM fuel cells. J Power Sources 2008;182:153–9.
[24] Zhou P, Wu CW, Ma GJ. Contact resistance prediction and structure optimization of bipolar plates. J Power Sources 2006;159:1115–22.
[25] Raunija TSK, Gautam RK, Bhradwaj VM, Nandikesan N, Shaneeth M, Sharma SC, et al. Low cost and rapidly processed randomly oriented carbon/carbon composite bipolar plate for PEM fuel cell. Fuel Cell 2016;16:801–9.
[26] Qiu D, Peng L, Yi P, Lai X. A micro contact model for electrical contact resistance prediction between roughness surface and carbon fiber paper. Int J Mech Sci 2017;124–125:37–47.
[27] Stock SR. X-Ray microtomography of materials. Int Mater Rev 1999;44:141–64.
[28] Stock SR. Recent advances in X-Ray microtomography applied to materials. Int Mater Rev 2008;53:129–81.
[29] Salvo L, Cloetens P, Maire E, Zabler S, Blandin JJ, Buffière JY, et al. X-Ray micro-tomography an attractive characterisation technique in materials science. Nucl Instrum Methods Phys Res Sect B Beam Interact Mater Atoms 2003;200:273–86.
[30] Garcea SC, Wang Y, Withers PJ. X-Ray computed tomography of polymer composites. Compos Sci Technol 2018;156:305–19.
[31] Czabaj MW, Riccio ML, Whitacre WW. Numerical reconstruction of graphite/epoxy composite microstructure based on sub-micron resolution X-Ray computed tomography. Compos Sci Technol 2014;105:174–82.
[32] Naouar N, Vidal-Sallé E, Schneider J, Maire E, Boisse P. Meso-scale FE analyses of textile composite reinforcement deformation based on X-Ray computed tomography. Compos Struct 2014;116:165–76.
[33] Pilinski N, Krishnan NN, Satola B, Rastedt M, Dyck A, Wagner P. Comparison of carbon based bipolar plate materials for polymer electrolyte membrane fuel cells. ECS Transactions 2018;86:315–27.
[34] Kakati BK, Sathiyamoorthy D, Verma A. Electrochemical and mechanical behavior of carbon composite bipolar plate for fuel cell. Int J Hydrogen Energy 2010;35:4185–94.
[35] Dhakate SR, Sharma S, Chauhan N, Seth RK, Mathur RB. CNTs nanostructuring effect on the properties of graphite composite bipolar plate. Int J Hydrogen Energy 2010;35:4195–200.
[36] Cunningham N, Lefèvre M, Lebrun G, Dodelet J-P. Measuring the through-plane electrical resistivity of bipolar plates (apparatus and methods). J Power Sources 2005;143:93–102.
[37] Sadeghifar H. In-plane and through-plane electrical conductivities and contact resistances of a Mercedes-Benz catalyst-coated membrane, gas diffusion and micro-porous layers and a Ballard graphite bipolar plate: impact of

humidity, compressive load and polytetrafluoroethylene. Energy Convers Manag 2017;154:191–202.

[38] Sow PK, Prass S, Kalisvaart P, Mérida W. Deconvolution of electrical contact and bulk resistance of gas diffusion layers for fuel cell applications. Int J Hydrogen Energy 2015;40:2850–61.

[39] Qiu D, Janßen H, Peng L, Irmscher P, Lai X, Lehnert W. Electrical resistance and microstructure of typical gas diffusion layers for proton exchange membrane fuel cell under compression. Appl Energy 2018;231:127–37.